

Carrier localization in III-nitride versus conventional III-V semiconductors: A study on the effects of alloy disorder using landscape theory and the Schrödinger equation


Tsung-Yin Tsai,^{1,2,§} Kai Shek Qwah^{1,*}, Jean-Philippe Banon³, Marcel Filoche^{3,4},
Claude Weisbuch^{1,3}, Yuh-Renn Wu^{2,†} and James S. Speck^{1,‡}

¹Materials Department, University of California, Santa Barbara, California 93106, USA

²Graduate Institute of Photonics and Optoelectronics and Department of Electrical Engineering, National Taiwan University, Taipei City 10617, Taiwan

³Laboratoire de Physique de la Matière Condensée, École Polytechnique, CNRS, Institut Polytechnique de Paris, 91120 Palaiseau, France

⁴Institut Langevin, ESPCI Paris, Université PSL, CNRS, 75005 Paris, France

 (Received 3 March 2023; revised 10 August 2023; accepted 12 September 2023; published 26 October 2023)

Semiconductor devices often require band-gap engineering, which in turn requires the use of alloys and the tuning of their composition to achieve the required electrical or optical behavior. While their compositional fluctuations are generally treated as a perturbation in most conventional III-V semiconductors, the effects of alloy disorder are much more significant in the III-nitrides. Here, the effects of alloy disorder on carrier localization are compared for different III-V semiconductors, particularly for holes for which localization effects are more significant due to their heavier effective mass. This study is conducted using three-dimensional computation for III-V alloys with natural (random) compositional fluctuations. Given the complexity of the problem, we carry out the computations relying on a simplified Hamiltonian in the envelope wave-function approximation with a single heavy-hole valence band. We investigate the effects of compositional fluctuations on carrier localization using two methods. The first method, based on the localization landscape theory, is used to solve the localization landscape equations and obtain the effective potentials acting on carriers. This potential acts as a confining potential that predicts the regions of spatial localization of carriers, and thus allows a comparison of the effects of alloy fluctuations between the conventional III-V and the III-nitride semiconductors. We find that the effective potential of the III-nitride semiconductors exhibits much larger fluctuations compared to the other III-V semiconductors. This might point to a higher degree of carrier localization in the nitrides, particularly for holes. This is verified through the second method, solving Schrödinger's equation and obtaining the electron and hole wave functions. We find that for $\text{In}_x\text{Ga}_{1-x}\text{N}$ the electron wave functions are delocalized even for the ground state, whereas the low-energy hole states are localized. This is in contrast with the behavior of holes in the common alloy $\text{In}_x\text{Ga}_{1-x}\text{As}$, which are found to be always delocalized. Thus, our study shows the importance of accounting for alloy disorder in the nitrides.

DOI: [10.1103/PhysRevApplied.20.044069](https://doi.org/10.1103/PhysRevApplied.20.044069)

I. INTRODUCTION

Semiconductors have been a major driver of the digital revolution. Since the invention of integrated circuits, the semiconductor industry has been dominated by silicon (Si) due to the availability of a very high-quality dielectric layer (silicon dioxide), high thermal conductivity, and the use of low-power complementary metal oxide semiconductor circuitry. Despite their success in

electronic devices, silicon and germanium are both very inefficient light emitters, due to their indirect band gaps. Thus, III-V compound semiconductors, with their direct band gaps, are ideal candidates for light-emitting applications. Traditional III-V compound semiconductors such as gallium arsenide (GaAs) and indium phosphide (InP) have been used in many applications, including high-speed optical communication networks. Their properties have motivated the development of In-Ga-As-P infrared lasers [1] and photodetectors [2]. In the visible spectrum, III-nitride-based semiconductors have been the dominant material system due to their wider band gap. This has led to the development of the light-emitting diode (LED) for general lighting, displays, and automotive applications

[†]claytonqwah@gmail.com

*yrwu@ntu.edu.tw

‡speck@ucsb.edu

§Both authors contributed equally to the paper

[3,4]. However, many semiconductor devices cannot rely only on the use of binary compounds and often require band-gap engineering, which in turn requires the use of alloys. By alloying two different semiconductors and tuning their proportions, one can achieve the desired value of a physical characteristic, such as band gap. [5]

To study these materials, researchers use theoretical models to understand their physical behavior and predict their properties. For homogeneous crystalline inorganic semiconductors, one solves the Schrödinger equation for electrons in a suitable periodic potential. According to Bloch's theorem, the solutions are delocalized Bloch wave functions for charge carriers, and the band structure of the semiconductors is obtained using various methods such as the tight-binding approximation or the density-functional theory [6]. However, when one uses semiconductor alloys, these techniques cannot be applied in their simple forms as the constituent atoms are randomly distributed throughout the crystal lattice. This phenomenon of random atomic positions, known as alloy disorder, means that the carriers are exposed to a random potential instead of a periodic one, causing Bloch's theorem to break down. While for "classic" III-V material-based alloys the effect of the random potential appears to yield modified delocalized states, the large random potential occurring in nitride-based alloys can lead to localized hole states. Such localized hole states in $\text{In}_x\text{Ga}_{1-x}\text{N}$ have been predicted for a long time by Bellaïche *et al.* and Kent and Zunger [7,8] and more recently by Watson-Parris *et al.*, Schulz *et al.*, and Tanner *et al.* [9–11].

The present study is focused on understanding the differences between III-nitride and conventional III-V semiconductor alloys due to the larger band gaps of nitrides, which lead to larger electronic energy fluctuations and larger effective masses. We use a novel method known as the localization landscape (LL) theory to obtain an effective potential for the different semiconductor alloys [12]. The effective potential is a classical potential that describes, to a good approximation, the modification of the fluctuating potential for electrons or holes induced by quantum mechanics. It provides a useful potential that, when implemented in classical drift-diffusion equations, describes the percolation paths followed by carriers in disordered systems. This potential has been very effective at simulating vertical transport across structures with multiple quantum wells in LEDs [13] as well as unipolar p -type nitride heterostructures [14,15]. Besides that, solving the LL equation is much faster than solving the Schrödinger eigenvalue problem. Li *et al.* did an analysis on the computational demand of the method, where it was found that the time required to solve the Schrödinger equation for a fixed matrix size at each iteration step is slower by 3 orders of magnitude than the one required for the landscape equation [13].

In this paper, we first compare, using the LL theory, the effective potentials for the main III-V compounds and show how unique the III-N materials are, due to their large band gaps and their related large carrier effective masses. Second, through direct solution of the Schrödinger equation (in the one-band envelope approximation), we show the density of localized hole states and its asymmetry with respect to the alloy composition. The synergistic interplay of large band-gap differences and effective masses of the pure alloy compounds is clearly highlighted. The eventual impact of such localized hole states in devices is discussed.

II. DISORDERED ALLOY POTENTIAL AND STRUCTURE OF THE ELECTRONIC STATES

A prerequisite to any calculation of the behavior of carriers is the construction of a model for the random potential acting on carriers. In this work, we model the effect of the disordered potential on the electrons due to the compositional fluctuations of the alloy within the framework of the effective mass approximation [16,17].

The effective mass approximation assumes that the single-particle eigenfunctions $\phi_{c,v}(\mathbf{r})$ of the Hamiltonian can be written as the product of the periodic part of the Bloch wave $v_{\text{CB},\text{VB}}(\mathbf{r})$ for the corresponding homogenous (not alloyed) crystal, where the subscripts CB and VB correspond to the conduction band and valence band, and an envelope function $\psi_{c,v}(\mathbf{r})$,

$$\phi_{c,v}(\mathbf{r}) = \psi_{c,v}(\mathbf{r}) v_{\text{CB},\text{VB}}(\mathbf{r}), \quad (1)$$

satisfying an effective Schrödinger equation,

$$-\frac{\hbar^2}{2} \nabla \cdot \left[\frac{\nabla \psi_{c,v}(\mathbf{r})}{m_{c,v}(\mathbf{r})} \right] + E_{c,v}(\mathbf{r}) \psi_{c,v}(\mathbf{r}) = E \psi_{c,v}(\mathbf{r}), \quad (2)$$

where E denotes the eigenenergy, $E_{c,v}(\mathbf{r})$ denotes the band energy, and $m_{c,v}(\mathbf{r})$ denotes the effective mass. The subscripts c and v denote quantities associated with the conduction and valence band, respectively. Note that, since the effective mass approximation only applies to the states near the band extrema [i.e., conduction-band minimum (CBM) or valence-band maximum (VBM)], the periodic part of the Bloch wave $v_{\text{CB},\text{VB}}(\mathbf{r})$ changes slowly through the Brillouin zone and, thus, the variation of these functions with the wave vector near band extrema is small. The potentials $E_{c,v}(\mathbf{r})$ and effective masses $m_{c,v}(\mathbf{r})$ appearing in the Schrödinger equation [Eq. (2)] are assumed to vary slowly at the scale of the lattice constant and they are modeled as follows. First, atoms from the group III elements of the alloy, which we denote generically as A and B , are drawn at random and placed on the lattice sites hosting group III elements. In other words, for each lattice site for group III r_j , atom A may be drawn with probability $1 - x$, and atom

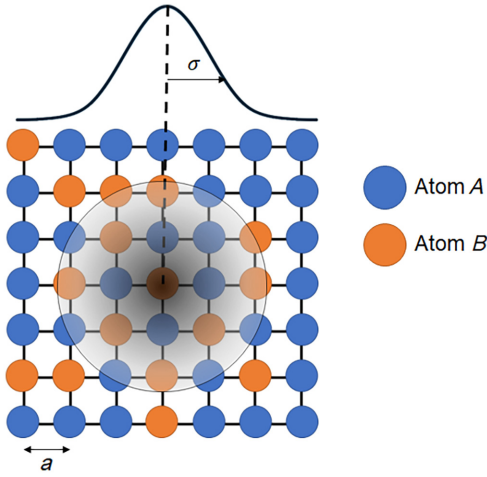


FIG. 1. Diagram illustrates the Gaussian averaging method of obtaining a composition profile for an alloy made up of atoms A and B .

B with probability x , where x is the average composition of the B_xA_{1-x} alloy. This defines a Bernoulli random variable x_j associated with the site r_j taking a value of 1 (atom B is drawn) or 0 (atom A is drawn). From the family of random variables x_j , we define a continuous random composition function $x(\mathbf{r})$ for any point \mathbf{r} (not necessarily on the lattice) as a Gaussian averaging of the discrete random variables x_j ,

$$x(\mathbf{r}) = \frac{\sum_j x_j \exp(-((\mathbf{r} - \mathbf{r}_j)^2/2\sigma^2))}{\sum_j \exp(-((\mathbf{r} - \mathbf{r}_j)^2/2\sigma^2))}. \quad (3)$$

Here, the parameter σ is a broadening length controlling the typical length scale over which the Gaussian averaging is performed, as readily seen from Eq. (3), and as illustrated in Fig. 1. In this work, the lattice is assumed to be cubic, with lattice constant a , for the sake of simplicity, although, in all generality, the actual lattice of the real crystal may also be considered [18]. The cubic lattice constant, a is chosen for each material to give the III-V elements the same volume as in the real crystal structures. The broadening length σ is chosen to be $\sigma = 2a$. The choice of $2a$ is made by many authors [9,13,19,20] and is justified in Refs. [5,13]. Figure 2(a) shows the computed structures with the x , y , z dimensions of $30 \times 30 \times 30 \text{ nm}^3$, as well as the top and bottom metal contacts. A low Si concentration of 10^{16} cm^{-3} is used to simulate unintentional donor doping in the structure. Figure 2(b) displays an example of the realization of the random composition function $x(\mathbf{r})$, denoted [In], for the $\text{In}_{0.3}\text{Ga}_{0.7}\text{N}$ alloy.

The conduction-band energy offset ΔE_c and valence-band energy offset ΔE_v are then calculated from the

random composition function x as follows:

$$E_g(\mathbf{r}) = x(\mathbf{r})E_{g,B} + (1 - x(\mathbf{r}))E_{g,A} + b(1 - x(\mathbf{r}))x(\mathbf{r}), \quad (4)$$

$$\Delta E_c = \gamma(E_{g,A} - E_{g,B}), \quad (5)$$

$$\Delta E_v = (1 - \gamma)(E_{g,A} - E_{g,B}). \quad (6)$$

In these equations, the parameter b is the so-called bowing parameter and γ is the band-offset ratio, i.e., the fraction of the band-gap difference at the interface or neighboring sites attributed to the conduction-band potential. The effective mass profiles are modeled as the harmonic average of the alloy parent materials for the sake of simplicity, i.e.,

$$\frac{1}{m_{c,v}(\mathbf{r})} = \frac{x(\mathbf{r})}{m_{c,v,B}} + \frac{1 - x(\mathbf{r})}{m_{c,v,A}}. \quad (7)$$

We use for both landscape and Schrödinger computations a single valence band with effective masses $m_{c,v,A,B}$ given by Eq. (7) with the heavy-hole masses of the pure compounds GaN and InN. The justification is given in the Supplemental Material section [21]. The values for the aforementioned material-specific parameters are summarized in Tables I and II. Figure 3 presents the variation with In composition of the band gaps, their derivatives, and the effective masses as a function of the average composition x for the different semiconductor alloys. The derivatives determine the amplitude of the band-gap energy fluctuations. The data show that the nitrides have much larger dE_g/dx , which results in the nitrides having larger band energy fluctuations. This in turn leads to effective potentials ($1/u_c$ and $1/u_v$) with higher fluctuations, due to their larger effective masses (see the following).

In addition to the random alloy atom contribution to the local band-gap energy, one needs to consider the electric potential originating from fixed (due to piezoelectric effects and ionized impurities) and mobile charges in the system, as they are not spread evenly across the structure and contribute to the potential values.

A three-dimensional (3D) continuum strain-stress model is adopted and solved using the finite-element method to calculate the strain distribution over the entire structure before solving the other equations. The strain is then used to obtain the piezoelectric polarization field \mathbf{P}^{PZ} using the formula

$$\mathbf{P}^{\text{PZ}} = [\mathbf{e}] \cdot [\boldsymbol{\varepsilon}] = \begin{bmatrix} e_{15}\varepsilon_{xz} \\ e_{15}\varepsilon_{yz} \\ e_{15}(\varepsilon_{xx} + \varepsilon_{yy}) + e_{33}\varepsilon_{zz} \end{bmatrix}, \quad (8)$$

where ε_{xx} , ε_{yy} , ε_{zz} are normal strains and ε_{yz} , ε_{zx} , ε_{xy} are shear strains. e_{15} , e_{31} , and e_{33} are the piezoelectric coefficients. The other terms of the piezoelectric tensor are zero due to the symmetry of wurtzite crystal structures.

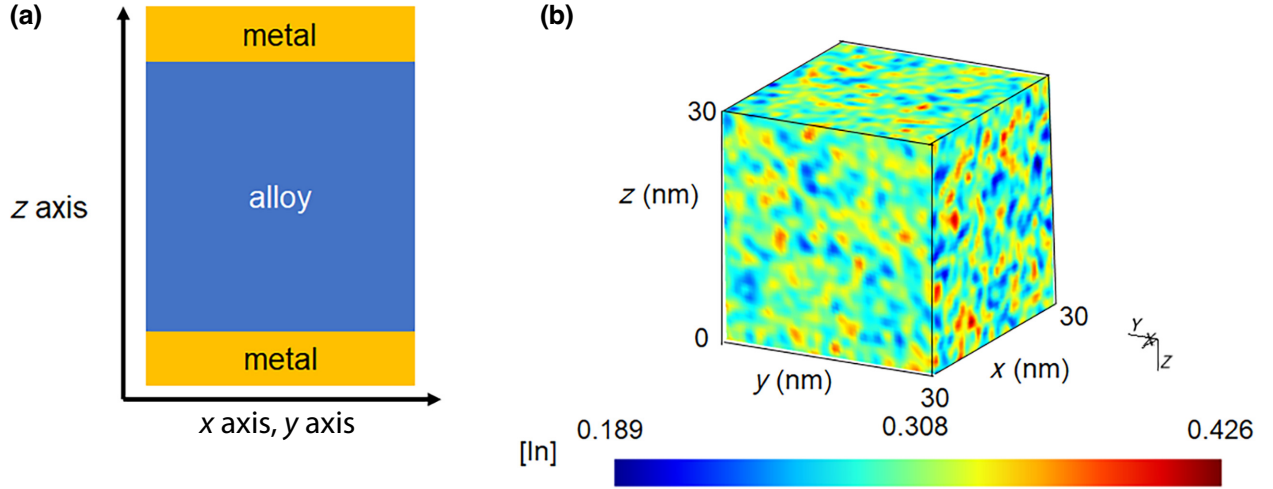


FIG. 2. (a) Schematic of the computed structure, showing the cross section in the x - z plane, (b) 3D map of the composition within the semiconductor for an average composition $x = 0.3$.

The spontaneous polarization \mathbf{P}^{SP} is then calculated by the following parabolic interpolation:

$$\mathbf{P}^{\text{SP}} = ax + b(1 - x) + cx(1 - x), \quad (9)$$

where a , b , and c are the spontaneous polarization coefficients for $\text{In}_x\text{Ga}_{1-x}\text{N}$. The values used in our computations are given in Tables III and IV.

The density of polarization charges, ρ_{pol} is then calculated by taking the divergence of the total polarization in

the space,

$$\rho_{\text{pol}} = \nabla \cdot \mathbf{P}_{\text{total}}, \quad (10)$$

$$\mathbf{P}_{\text{total}} = \mathbf{P}^{\text{SP}} + \mathbf{P}^{\text{PZ}}. \quad (11)$$

This value is then plugged into Poisson's equation and solved over each node of the structure. The Poisson equation is generally of the form

$$\nabla \cdot (\varepsilon(\mathbf{r})\nabla\varphi(\mathbf{r})) = e(n - p - N_D^+ + N_A^- \pm \rho_{\text{pol}}(\mathbf{r})), \quad (12)$$

where φ is the electrostatic potential; ε is the dielectric permittivity; e is the electron charge; n and p are the electron and hole carrier densities, respectively; and N_D^+ and

TABLE I. The longitudinal electron effective masses ($m_{e,c}^*$), transverse electron effective masses ($m_{e,x,y}^*$), heavy-hole effective masses (m_{hh}^*), lattice parameters (a), and band gaps (E_g) for different III-V semiconductors. Note for the wurtzite structure nitrides, the longitudinal direction is parallel to the c axis and the transverse directions are perpendicular to the c axis. For the conventional III-Vs, only an isotropic electron effective mass is used. This work focuses on the localization behavior of the low-energy holes, i.e., the heavy holes of the valence band; therefore, the landscape potential and wave function of holes shown in this work are for heavy holes. The approximation of a single heavy-hole band in nitrides is discussed in the Supplemental Material [21]. All of the values given are for the temperature of $T = 300$ K.

	$m_{e,c}^*$	$m_{e,x,y}^*$	m_{hh}^*	a (nm)	E_g (eV)
GaN	0.21	0.20	1.87	0.283	3.437
InN	0.070	0.070	1.61	0.283	0.61
AlN	0.32	0.3	2.68	0.283	6
GaAs	0.067		0.45	0.356	1.42
InAs	0.027		0.26	0.382	0.354
AlAs (Γ)	0.146		0.51	0.357	2.67
InP	0.073		0.46	0.370	1.35
GaP (Γ)	0.09		0.79	0.343	2.76

$\Gamma = \Gamma$ -band in the band structure.

TABLE II. Band-gap bowing parameters, γ (the band-offset ratio, i.e., the fraction of the band-gap difference attributed to the conduction-band potential), as well as conduction-band and valence-band offsets [CBO:VBO (%), percentage of band-gap differences in the corresponding band] for the different III-V alloys.

	Bowing parameter b (eV)	γ	CBO:VBO (%)
$\text{In}_x\text{Ga}_{1-x}\text{N}$	-2	0.63	InN:GaN 63:37
$\text{Al}_x\text{Ga}_{1-x}\text{N}$	-0.8	0.63	AlN:GaN 63:37
$\text{In}_x\text{Ga}_{1-x}\text{As}$	-0.58	0.78	InAs:GaAs 78:22
$\text{Al}_x\text{Ga}_{1-x}\text{As}$	-0.37	0.57	AlAs:GaAs 57:43
$\text{In}_x\text{Ga}_{1-x}\text{P}$	-0.65	0.81	InP:GaP 81:19

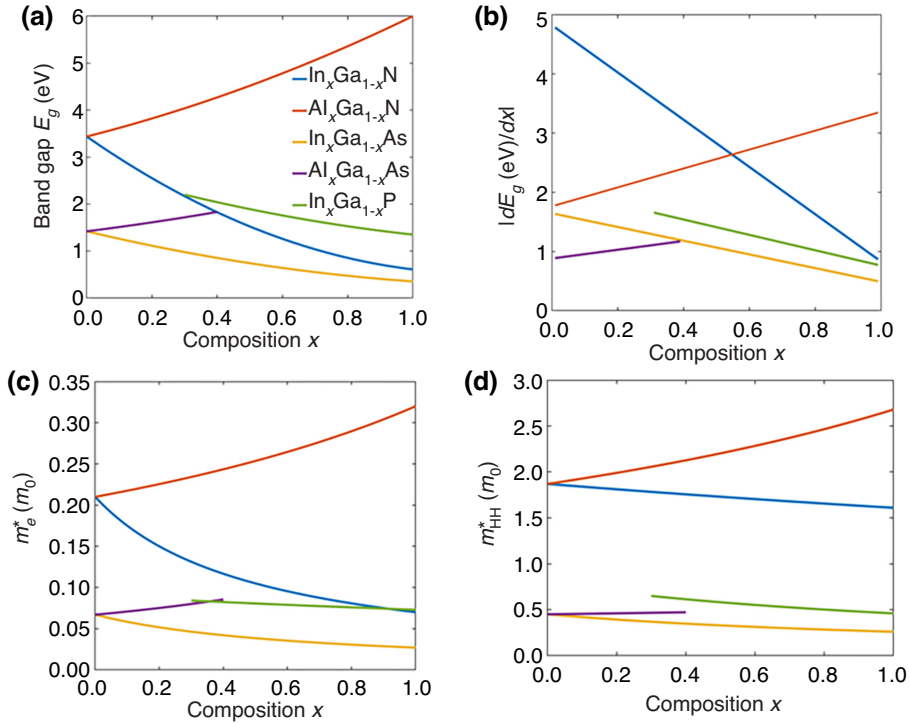


FIG. 3. Dependence of (a) band gap; (b) change in band gap as a function of composition; (c) effective electron mass; and (d) effective heavy-hole mass on alloy composition for common semiconductor alloys. These are plotted only for compositions that correspond to direct band gaps. Note the large differences in parameters for the different materials, as well as the larger band-gap slopes and effective hole masses for nitrides, resulting in large disorder effects.

N_A^- are the ionized donor and acceptor densities, respectively. In this study, we treat a uniform background value for $N_D = 1 \times 10^{16} \text{ cm}^{-3}$ with an ionization energy of about 25 meV to simulate unintentional doping, particularly for the nitrides. Furthermore, we do not consider acceptors in this study. We note that the data with and without the background impurity doping are essentially the same and thus, it makes no quantitative difference to the overall results of the study.

The conduction-band (E_c) and valence-band (E_v) potentials are then directly obtained through

$$E_c(\mathbf{r}) = -e\varphi(\mathbf{r}) + \gamma E_g(\mathbf{r}), \quad (13)$$

$$E_v(\mathbf{r}) = E_c(\mathbf{r}) - E_g(\mathbf{r}), \quad (14)$$

where γ is the band-offset ratio found in Table II. Looking at Eq. (12), one notes that the presence of polarization charges plays a significant role in determining the shape of the conduction- and valence-band profiles and, consequently, the localization behavior of carriers in our structure.

TABLE III. Piezoelectric coefficients used in calculations.

	e_{33} (C/cm ²)	e_{31} (C/cm ²)	e_{15} (C/cm ²)
GaN	0.73	-0.49	-0.40
InN	0.73	-0.49	-0.40

III. LOCALIZATION LANDSCAPE AND THE EFFECTIVE POTENTIAL

The first approach to assess the localization properties of electrons and holes in the disordered alloy is through the computation of the effective potential defined from the so-called LL [12,13,22]. The LL $u_{c,v}(\mathbf{r})$ are defined by

$$-\frac{\hbar^2}{2} \nabla \cdot \left[\frac{\nabla u_c(\mathbf{r})}{m_c(\mathbf{r})} \right] + (E_c(\mathbf{r}) - E_{c,\min})u_c(\mathbf{r}) = 1, \quad (15)$$

$$\frac{\hbar^2}{2} \nabla \cdot \left[\frac{\nabla u_v(\mathbf{r})}{m_v(\mathbf{r})} \right] - (E_v(\mathbf{r}) - E_{v,\max})u_v(\mathbf{r}) = 1. \quad (16)$$

As can be seen from these equations, the LL $u_c(\mathbf{r})$ or $u_v(\mathbf{r})$ is a solution of the partial differential equation associated with the Hamiltonian operator of the Schrödinger and with a uniform source term equal to 1. It has been shown to provide relevant insights about the spatial and spectral properties of the band-edge states (localized or not) [22,23]. In particular, it was shown in Ref. [23] that one may define effective potentials from the reciprocal of

TABLE IV. Spontaneous polarization coefficients.

	a (C/cm ²)	b (C/cm ²)	c (C/cm ²)
In _x Ga _{1-x} N	-0.042	-0.034	0.037

the LL, as

$$\frac{1}{u_c}^{(\text{eff})}(\mathbf{r}) = E_{c,\text{min}} + \frac{1}{u_c(\mathbf{r})}, \quad (17)$$

$$\frac{1}{u_v}^{(\text{eff})}(\mathbf{r}) = E_{v,\text{max}} - \frac{1}{u_v(\mathbf{r})}. \quad (18)$$

The effective potentials are smoothed versions of the original potentials $E_{c,v}(\mathbf{r})$ at a suitable scale dictated by the underlying eigenstates of the Hamiltonian. They can be seen as semiclassical potentials that, to some extent, account for quantum confinement and tunneling effects. In the following, since we are primarily concerned with the fluctuations of the effective potentials, they are simply denoted $1/u_{c,v}(\mathbf{r})$ and the specific reference of energy for their graphical representation is specified.

IV. NUMERICAL METHODS

We use freely available software, known as the 3D drift-diffusion charge control (3D DDCC) solver (see Refs. [13,24]) to solve the Schrödinger and LL equations. First, we solve Poisson's equation [Eq. (12)] to obtain $E_c(\mathbf{r})$ and $E_v(\mathbf{r})$, which are then inserted into the landscape equations as input parameters to obtain landscape potentials. The LL equations are solved using the Neumann boundary conditions in the z direction and periodic boundary conditions in the x and y directions. Poisson's equation and the landscape equation are then solved iteratively until the maximum error of electrostatic potential between two consecutive iterations is less than 10^{-5} eV.

In the case of the wave functions, the $E_c(\mathbf{r})$ and $E_v(\mathbf{r})$ obtained from Poisson's equation are then used as input parameters in the Schrödinger equation to obtain the eigenenergies and wave function, with the same boundary conditions as previously mentioned. The Schrödinger eigenvalue problems are solved using the linear algebra package (LAPACK) implemented in FORTRAN [25].

V. STATISTICAL ANALYSIS OF THE FLUCTUATIONS OF THE BAND AND EFFECTIVE POTENTIALS: RESULTS FROM THE LOCALIZATION LANDSCAPE THEORY

The first step towards the comparison of the localization properties of the carriers in the different semiconductor alloys is the study of the statistical properties of the fluctuations of the potentials and effective potentials. Figure 4 presents, in succession, the two-dimensional (2D) sectional maps of the composition [In], the fluctuations of the conduction-band potential $E_c(\mathbf{r})$, and the fluctuations of the effective potential $1/u_c(\mathbf{r})$ for an $\text{In}_{0.3}\text{Ga}_{0.7}\text{N}$ alloy. One can observe the reduced fluctuations of the effective potential $1/u_c(\mathbf{r})$ compared to the fluctuations of the conduction-band potential $E_c(\mathbf{r})$. Figures 5(a) and 5(b)

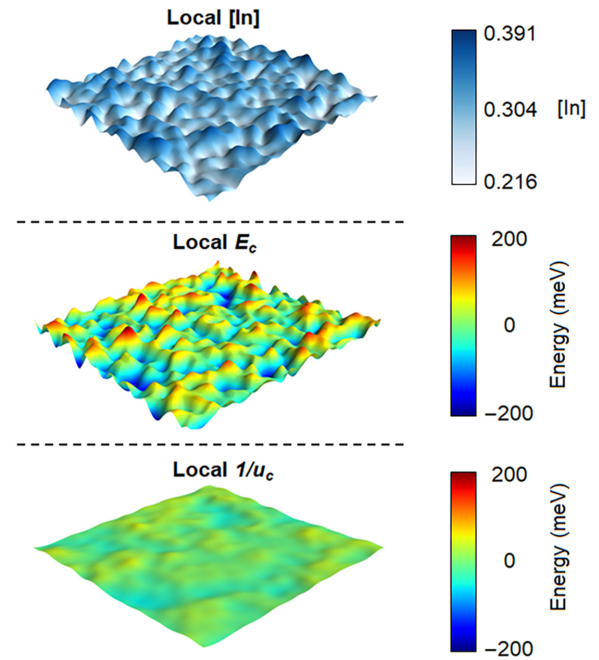


FIG. 4. (a) Sectional map of local compositional fluctuations for a realization of a random 30% alloy; all random alloys have the same compositional map at a given composition; (b) sectional map of the local conduction-band extremum of the realization of a $\text{In}_{0.30}\text{Ga}_{0.7}\text{N}$ alloy; (c) sectional map of the local effective potential $1/u_c$ for the same realization obtained by the LL theory. The scales on the right correspond to the compositional or energy fluctuation maps, with the energies shifted to their mean value.

display the fluctuations of the band potential $E_{c,v}(\mathbf{r})$ and the fluctuations of the effective potential $1/u_{c,v}(\mathbf{r})$ for the main III-V alloys $\text{In}_x\text{Ga}_{1-x}\text{N}$, $\text{In}_x\text{Ga}_{1-x}\text{As}$, $\text{Al}_x\text{Ga}_{1-x}\text{N}$, $\text{Al}_x\text{Ga}_{1-x}\text{As}$, and $\text{In}_x\text{Ga}_{1-x}\text{P}$.

There are no striking differences between the magnitudes of band potential fluctuations in the different materials of Fig. 5(a), with the nitrides displaying somewhat larger fluctuations compared to the other semiconductors. This is due to their larger band-gap variations with composition, as the compositional fluctuations are the same for random alloys with the same compositions. In Fig. 5(b), it is shown that the different alloys' effective potential maps have smaller fluctuations than the original band extrema fluctuations. However, the effective potentials of nitrides show much larger fluctuations compared to the more common III-V semiconductor alloys. This is due to another ingredient that plays a major role in the fluctuations of the nitrides' effective potentials, which is their larger effective masses. These heavier masses increase the confinement of carriers and reduce their ability to tunnel through the barriers in the fluctuating potential, which in turn increases the fluctuations of the effective quantum potential (Fig. 6). Both components (i.e., the band extrema variations and effective masses) are larger in the nitrides compared to the

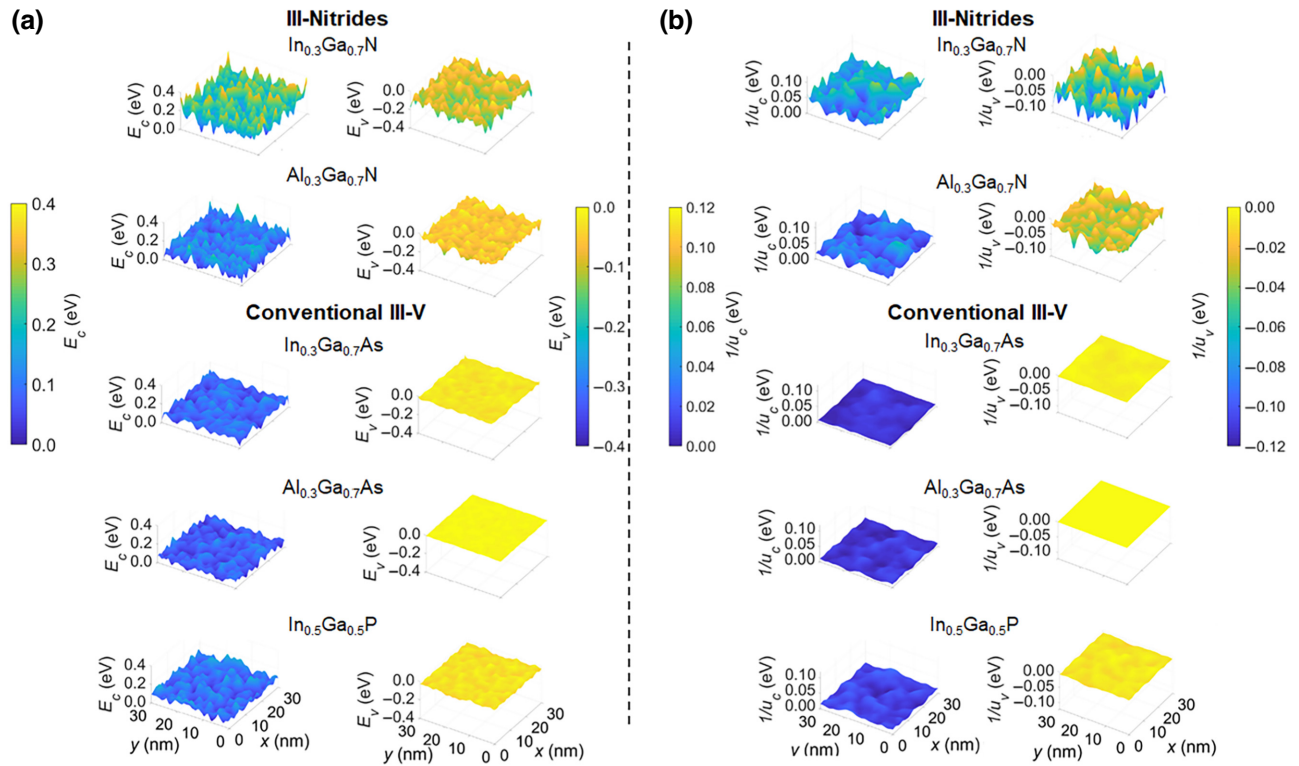


FIG. 5. (a) 2D sectional maps of CBM and VBM for different semiconductor alloys in an x - y plane in the middle of the structure. Maps of compositional fluctuations are not shown as they are the same for random alloys with the same relative composition (30% here), except for $\text{In}_{0.5}\text{Ga}_{0.5}\text{P}$ with 50% composition. The zero-energy references for E_c and E_v are, respectively, the minimum and maximum values of band extrema for a specific realization. (b) 2D cross sections of the corresponding effective potentials computed by the LL equations. Compare the size of effective energy fluctuations with those of the originating band extrema energy fluctuations (note the different energy scales). The left and right color bars correspond to each column of the sectional maps.

other III-V semiconductors, as large band gaps are usually associated with both large energy fluctuations and large effective masses, as calculated from $\mathbf{k} \cdot \mathbf{p}$ theory [26,27].

We then conduct a more detailed analysis on $\text{In}_x\text{Ga}_{1-x}\text{N}$ and $\text{In}_x\text{Ga}_{1-x}\text{As}$ at $x=0.30$. $\text{In}_x\text{Ga}_{1-x}\text{As}$ is chosen as a reference for the behavior in the conventional III-V semiconductors. The choice of setting the indium composition to 30% is made as it is the extreme for experimental coherent planar growth, particularly for $\text{In}_x\text{Ga}_{1-x}\text{N}$. This choice is further justified later in this study, as it is also the composition with the highest energy fluctuations.

To quantify the magnitude of the fluctuations of $[\text{In}]$, $E_{c,v}(\mathbf{r})$ and $1/u_{c,v}(\mathbf{r})$ frequency distribution plots are made. To produce these plots, the number of grid points that fall within a certain bin value (this value would be either the composition, band energy, or effective potential value at that point) are counted and binned. For all the distribution plots, the number of grid points is normalized to the total number of computation nodes, which is 226 981. The number of grid points is 61 in the x , y , and z directions.

To quantify the fluctuations of the different variables and quantities, we evaluate their standard deviation. The standard deviation of $1/u_c$ is illustrated in Fig. 7.

The frequency distribution for the indium content, band extrema, and effective landscape potentials ($1/u_{c,v}$) are shown in Fig. 8. The figure shows that both alloys follow the same distribution, which is expected as it is known that the atoms of random alloys are generated identically, with the only difference being in the lattice constant size. However, the conduction-band (E_c) and valence-band (E_v) energy distributions are narrower in $\text{In}_x\text{Ga}_{1-x}\text{As}$ than in $\text{In}_x\text{Ga}_{1-x}\text{N}$. This is due to the smaller band-gap differences between GaAs and InAs (1.066 eV) in comparison with GaN and InN (2.827 eV). A similar trend is seen in the landscape potentials for electrons $1/u_c$ and holes $1/u_v$. It is also observed that the E_c and E_v distributions are much wider than their corresponding landscape potentials, as the landscape equation smooths the energy fluctuations and reduces their size, as discussed previously.

The standard deviations of E_c , E_v , $1/u_c$, and $1/u_v$ are shown in Fig. 9 for the different indium compositions. It is observed that $\text{In}_x\text{Ga}_{1-x}\text{As}$ consistently shows narrower distributions for the different band energy potentials over indium composition compared with $\text{In}_x\text{Ga}_{1-x}\text{N}$, which in turn corresponds to smaller band-gap extrema fluctuations seen by the carriers. Consequently, disorder effects

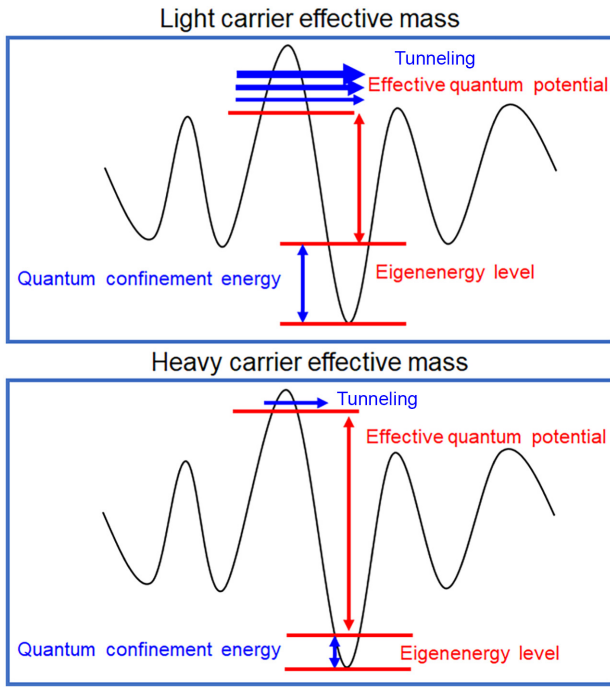


FIG. 6. Schematics of the impact of the effective mass on the effective potential: a lighter mass (top) both increases the confinement energy and decreases the tunneling barrier, which both diminish the effective potential experienced by carriers.

are more pronounced in $\text{In}_x\text{Ga}_{1-x}\text{N}$, such as for percolative transport through multilayers [13], and carriers are more likely to be localized in $\text{In}_x\text{Ga}_{1-x}\text{N}$ compared with $\text{In}_x\text{Ga}_{1-x}\text{As}$ (see the following). Another interesting observation is that, while the fluctuations of the conduction band E_c are larger than those of the valence band E_v for $\text{In}_x\text{Ga}_{1-x}\text{N}$, their corresponding effective potentials show the reverse behavior. This means that, if one looks only at band offsets and band gaps, one would predict that electrons are more likely to localize than holes. It is only by looking at the effective potential, $1/u_{c,v}$ that one can see that holes are more likely to localize. This is due to their deeper effective potential fluctuations and their heavier effective mass which, in the LL treatment, lead to

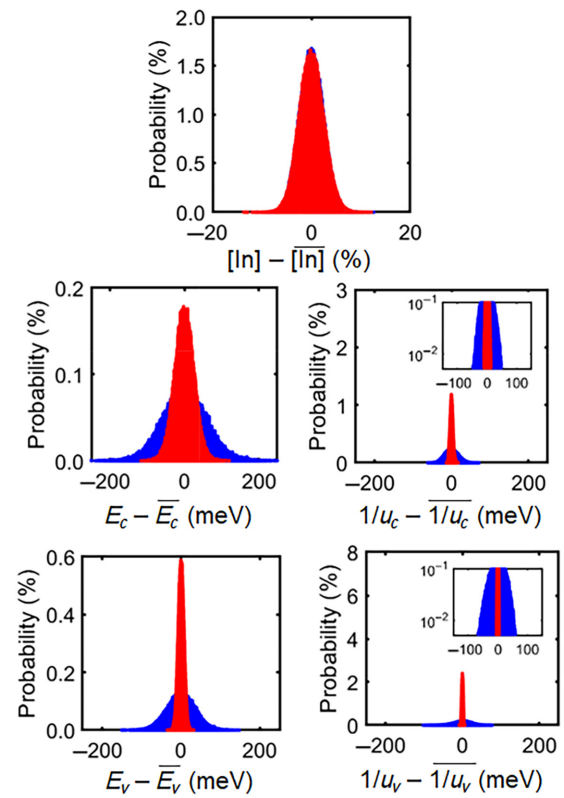


FIG. 8. Frequency distribution plots of the indium composition and conduction-band and valence-band extrema, as well as their corresponding effective landscape potentials $1/u$ (red, $\text{In}_x\text{Ga}_{1-x}\text{As}$; blue, $\text{In}_x\text{Ga}_{1-x}\text{N}$; $[\text{In}] = 30\%$). The x -axis values are shifted to zero by subtracting the mean value. The bin size is set to be 0.1% for the In composition distribution while the bin size for the band energies and their corresponding landscape potentials is 0.1 meV.

shorter Agmon distances [10] and hence, to more localized states. The corresponding effect of the heavier hole in the Schrödinger equation computation is the smaller confinement energy within a low-energy well caused by fluctuations and weaker tunneling between lower-energy regions, which both increase the effective fluctuation energy as discussed in Fig. 6.

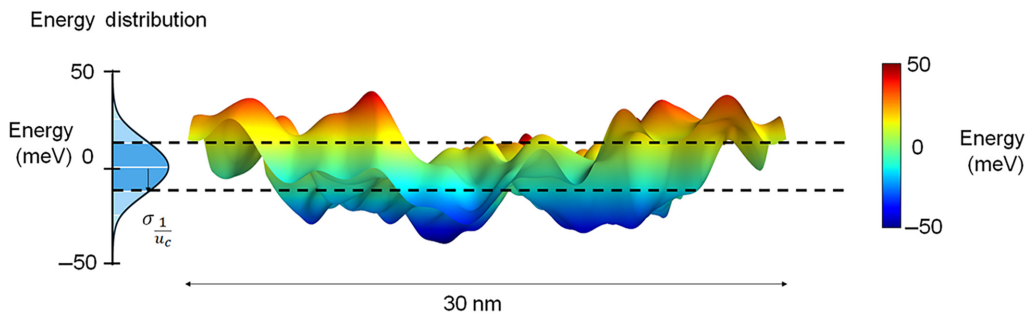


FIG. 7. Diagram showing how the average fluctuations of an effective energy landscape correspond to the standard deviation of the effective energy distribution, σ_{1/u_c} for the same landscape.

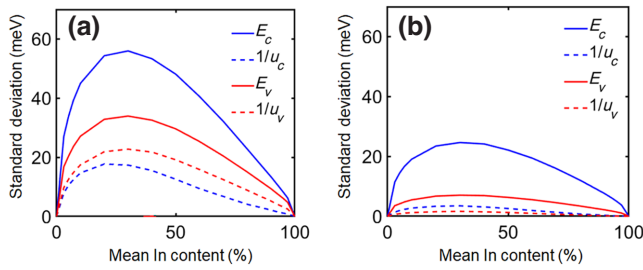


FIG. 9. Dependence of the standard deviation in the band-gap extrema and effective potentials on alloy composition x for (a) $\text{In}_x\text{Ga}_{1-x}\text{N}$ and (b) $\text{In}_x\text{Ga}_{1-x}\text{As}$. For all compositions, the effective potential fluctuations are reduced compared to those of the starting potentials. Note that the reduction in the fluctuations from E_c to $1/u_c$ is smaller than the reduction from E_v to $1/u_v$.

The standard band-gap extrema fluctuations have their highest value for the approximate 30% indium composition. This is a result of two factors (Fig. 10): First, the alloy compositional fluctuations are largest at 50% indium composition for both semiconductors. Second, the band gap has the steepest slope with respect to In concentration at the lower indium compositions. It is the combination of these two factors that causes the peak width of the potential distributions to be at around 30% indium composition, as illustrated in Fig. 9.

VI. ANALYSIS OF LOCALIZATION PROPERTIES OF THE EIGENSTATES: RESULTS FROM SOLVING THE 3D SCHRÖDINGER EQUATION

In addition to the landscape equation, the full Schrödinger equation [Eq. (2)] is solved to determine the electron and hole eigenstates and eigenfunctions, although at a much larger computational cost [13]. Solving the Schrödinger equation allows us to observe the transition from localized to delocalized eigenstates with increasing

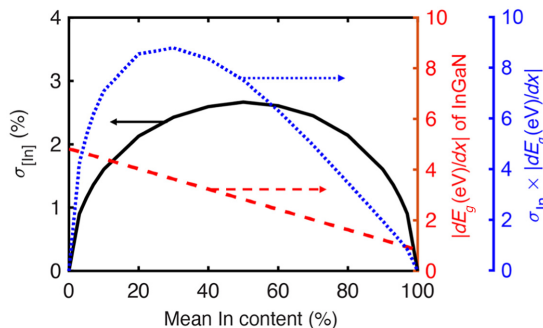


FIG. 10. Dependence of natural alloy composition fluctuations $\sigma_{[\text{In}]}$ (black curve), band-gap change dE_g/dx (red), and their product $\sigma_{\text{band gap}} = \sigma_{[\text{In}]}(dE_g/dx)$ (blue) on indium composition for $\text{In}_x\text{Ga}_{1-x}\text{N}$ alloys. The largest band-gap fluctuations $\sigma_{\text{band gap}}$ are at about 30% indium composition.

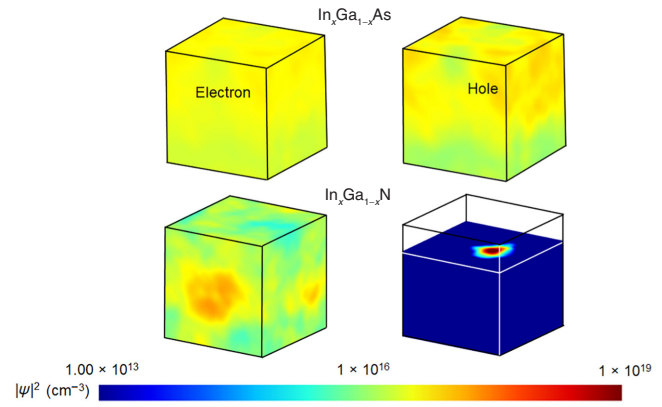


FIG. 11. 3D plots of the ground-state electron and hole probability densities for $\text{In}_{0.3}\text{Ga}_{0.7}\text{N}$ and $\text{In}_{0.3}\text{Ga}_{0.7}\text{As}$. The dimensions of the boxes are $30 \times 30 \times 30 \text{ nm}^3$ in the x , y , and z directions, respectively.

eigenenergy. This serves as a good reference for our computations with LL theory. To save computation time and to focus on the localization behavior in $\text{In}_x\text{Ga}_{1-x}\text{N}$ and $\text{In}_x\text{Ga}_{1-x}\text{As}$, the 3D Schrödinger solver is only used to determine the eigenvalues from the lowest energy value up to the highest energy value of the spatially varying band extrema for a given alloy realization (E_c or E_v).

Figure 11 shows the probability density of the ground-state eigenfunctions for electrons and holes for $\text{In}_x\text{Ga}_{1-x}\text{N}$ and $\text{In}_x\text{Ga}_{1-x}\text{As}$. The electron and hole ground-state eigenfunctions for $\text{In}_x\text{Ga}_{1-x}\text{As}$ are shown to be completely delocalized, as evidenced by the spread of their probability densities across the structure. However, in the $\text{In}_x\text{Ga}_{1-x}\text{N}$ structure, while the electron ground state is shown to be delocalized, the hole ground state is very localized. This is seen in Fig. 11, with the $\text{In}_x\text{Ga}_{1-x}\text{N}$ hole ground state having a large probability density over a restricted volume. This difference in behavior is due to the large effective mass for holes in the nitrides. As mentioned above, such a result has been demonstrated in previous studies on quantum wells [9,10,28–30] and in bulk $\text{In}_x\text{Ga}_{1-x}\text{N}$ [7,8,28]. We note that one finds two definitions of the concept of localization in the literature: For some authors, localization can mean partial localization of the wave function in some regions while the state is unbound and extends to infinity [7,27]. A more generally used definition, which is the one used in this study, is for quantum states that are bound within the band gap, with wave functions decaying exponentially. This is best described by the use of the participation ratio of a wave function, described hereafter.

Let us first discuss such a difference in localization properties of electrons and holes, as it is not obvious from the values of their effective potential fluctuations in Fig. 9. The exponential decay of a localized eigenstate between minima of the effective potential is governed by an exponentially decaying function, with a decay rate that scales

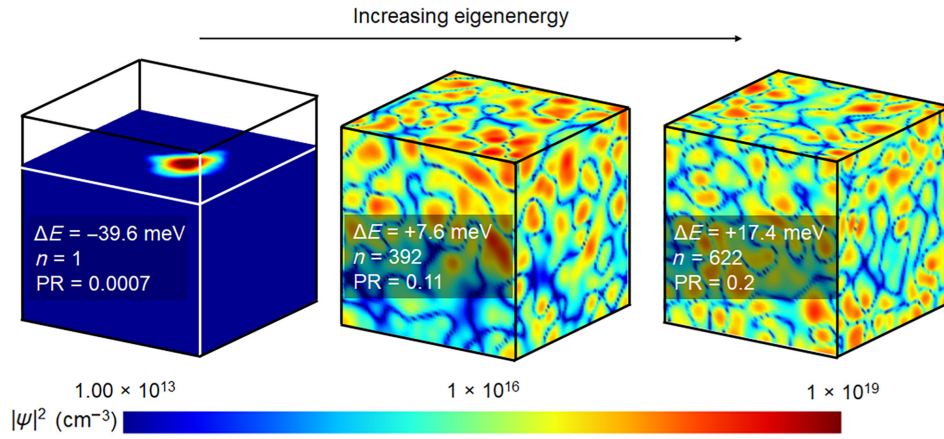


FIG. 12. 3D plots of selected hole probability densities for $\text{In}_x\text{Ga}_{1-x}\text{N}$ with increasing eigenenergy. In these examples, n corresponds to the specific eigenfunction (where $n = 1$ corresponds to the ground state), ΔE is eigenenergy relative to the average VB maximum, and PR corresponds to the participation ratio of the specific eigenfunction.

as $\sqrt{m^*}$. This is also known as the Agmon distance [23]. Thus, at the scales considered here, electron eigenstates do not decay sufficiently fast between the wells of the effective potential to be localized due to their light mass, whereas low-energy heavier-hole eigenstates do.

Figure 12 shows the plots of selected hole eigenstates with increasing eigenenergies. ΔE is defined as the eigenenergy value subtracted from the average valence-band maximum. The index n refers to the n th eigenstate. PR refers to the participation ratio of the eigenstate ψ_n , which we discuss in the following. As the energy increases, the hole becomes increasingly delocalized. An interesting observation to be made is that the structure of the highly excited eigenstate is strongly reminiscent of the compositional fluctuations of the alloy [see Fig. 2(b)], even when the hole eigenstates are delocalized. This is in contrast with the electron eigenstates, which show a negligible imprint of the alloy fluctuations. This is due to a fundamental property of the Schrödinger equation, which is that the eigenstates are orthogonal to each other. This causes the delocalized states to have an imprint of the lower-energy localized states, as the spatial overlap between eigenstates must be zero,

$$\int_{\Omega} \psi_n^*(\mathbf{r})\psi_m(\mathbf{r})d\Omega = \delta_{nm} \quad (19)$$

where $\psi_n(\mathbf{r})$ is an eigenfunction of the Hamiltonian and δ_{nm} is the Kronecker delta function. This can also be seen when the Schrödinger equation is expressed as

$$\frac{\nabla^2\psi_n(\mathbf{r})}{\psi_n(\mathbf{r})} = \frac{2m^*(V(\mathbf{r}) - E_n)}{\hbar^2}, \quad (20)$$

where one can observe that all eigenstates have the same map of $(\nabla^2\psi_n(\mathbf{r})) / (\psi_n(\mathbf{r}))$, only determined by the product of the mass times the potential $V(r)$.

It is not easy to visually assess the degree of localization for wave functions that cover a sizeable portion of the computing volume. One method to quantify the degree of localization for each eigenstate, which has been a challenge in disordered systems, is to introduce the participation ratio, PR [31]. It is given by

$$PR = \frac{1}{|\Omega|} \frac{(\iiint_{\Omega} \psi^2 dx dy dz)^2}{\iiint_{\Omega} \psi^4 dx dy dz}, \quad (21)$$

where Ω is the volume of the structure. For a wave function that is constant throughout the volume, with either periodic or Neumann boundary conditions, the PR is equal to 1,

$$PR = \frac{1}{|\Omega|} \frac{(\iiint_{\Omega} A^2 dx dy dz)^2}{\iiint_{\Omega} A^4 dx dy dz} = 1. \quad (22)$$

This quantity clearly represents the extent to which the wave function occupies the computation volume, with its value increasing with the degree of delocalization. One has to note that for a constant potential, and for the boundary conditions considered in this work, only the ground state has $PR = 1$. The eigenstates that are constant in two directions (and sinusoidal in the last one) have $PR = 2/3$, eigenstates constant in one direction only have $PR = (2/3)^2 \approx 0.44$, and all other eigenstates (products of sine waves) have $PR = (2/3)^3 \approx 0.3$. These are the values that are observed in Figure 13 for the PR s of electrons and holes in $\text{In}_x\text{Ga}_{1-x}\text{As}$. This is due to the relative weakness of the potential and of the effective mass, and hence the ground-state wave function is roughly constant for the considered boundary conditions. This only happens in $\text{In}_x\text{Ga}_{1-x}\text{As}$, as the low effective mass and small band-gap variations with composition result in the eigenstates behaving as delocalized waves.

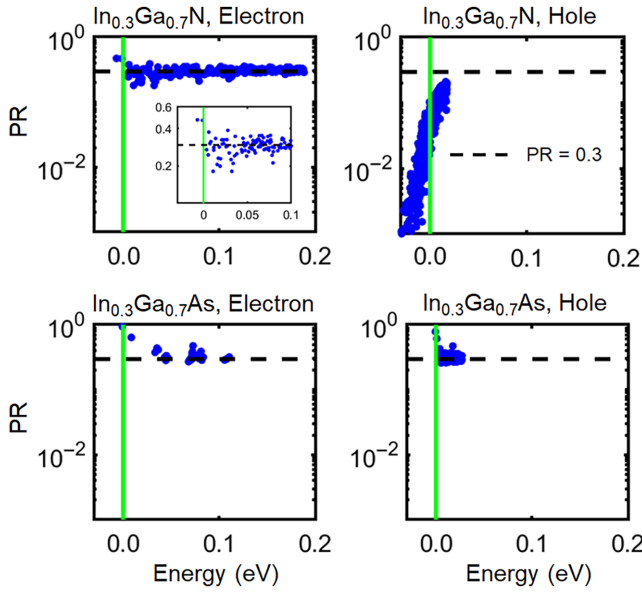


FIG. 13. The dependence of the participation ratio (PR) value on the eigenenergy for electron and hole eigenstates for $\text{In}_x\text{Ga}_{1-x}\text{N}$ and $\text{In}_x\text{Ga}_{1-x}\text{As}$. The vertical green line represents the averaged conduction-band minimum (for electrons) and the averaged valence-band maximum (for holes) over the structure. The horizontal dashed lines represent the PR value of 0.3. The inset shows an enlarged view of the low-energy electron eigenstates.

In the case of $\text{In}_{0.3}\text{Ga}_{0.7}\text{N}$, the PR of electron eigenstates is around 0.3. For holes, several states exhibit a low PR , increasing with energy. However, their PR does not quite reach a value of order 1 or 0.3, characteristic of fully delocalized states, due to the higher lying eigenstates having an imprint of the lower localized eigenstates, which is a consequence of the orthogonality of the eigenstates, again diminishing the volume accessible to the hole wave functions. This comparison between electrons and holes in $\text{In}_{0.3}\text{Ga}_{0.7}\text{N}$ shows that the effective mass plays an essential role in determining the localization behavior of carriers for somewhat similar effective potential fluctuations as in $\text{In}_{0.3}\text{Ga}_{0.7}\text{N}$ for electrons and holes (Fig. 9).

Following that, the PR is calculated for hole eigenstates of different $\text{In}_x\text{Ga}_{1-x}\text{N}$ compositions to predict which value of In composition would lead to most localization (Fig. 14). Additionally, the plots are also made for the density of states that fall in a certain range of energy values in order to track the number of states that are localized (Fig. 14). It is observed that, for the lowest and highest In compositions, there are fewer localized states, in particular at larger values of x . This is due the asymmetry of the $\sigma_{\text{band gap}} = \sigma_{[\text{In}]} \times (dE_g/dx)$ curve (Fig. 10) and the lighter hole mass at high In concentration (Fig. 3). It appears clearly that, although they have equivalent compositional fluctuations, the number of localized states for 10%

vs 90% and 30% vs 70% concentrations are very different. At 10% In, many lower-energy eigenstates have very low PR values, and thus can be considered as localized. As we increase the indium content to 30%, which corresponds to the largest fluctuations in the effective potential, there seems to be an overall reduction in the PR value for the hole eigenstates, which means that more states are strongly localized. This trend changes, with the average PR value increasing as the In composition increases beyond 50%. At 90% In composition, where the alloy is mostly InN, only the very lowest-energy hole eigenstates are found to be localized, with nearly all others being delocalized with a PR value of around 0.3. This tallies with the variation of the standard deviation of potentials of Fig. 9. It is also noted that, for every indium composition, most of the localized states are below the average value of valence-band energy E_v , meaning that these states are likely localized in a local minimum of the valence band. One can also observe that for the material with maximum disorder $\text{In}_{0.3}\text{Ga}_{0.7}\text{N}$, delocalized states have a PR value somewhat distant from the PR value of 1 for fully delocalized states (see inset in Fig. 14). This originates from the delocalized states seeing a large fraction of the volume as inaccessible due to the many localized states to which they are orthogonal.

Another way to look at localization is to use the PR to define a localization length. We define a characteristic localization length, ℓ , where

$$\ell = (\Omega PR)^{1/d}. \quad (23)$$

This length corresponds to the spatial extent of the eigenstate; the details of this metric can be found in the Supplemental Material section of this paper [21]. To illustrate the aspect of eigenstates for different hole localization lengths, plots of the 3D eigenstates are made for localization lengths from 3 to 10 nm in Fig. 15. The diagram shows the volume occupied by the wave function steadily increasing with the localization length. We can also determine from the plots a localization length of 5 nm above which we assume that wave functions are delocalized as, from this value on, the wave functions begin to spread to all the faces of the cube (Fig. 15).

Since the length of each side in our alloy is 30 nm, we can estimate an upper limit of the volumetric percentage of a localized state, i.e., the PR for a localization length of 5 nm, as

$$PR = \frac{\text{Volume of localized state}}{\text{Total volume}} \sim \frac{(5 \text{ nm})^3}{(30 \text{ nm})^3} = 0.004. \quad (24)$$

Therefore, a localized state occupies less than 0.4% of the total volume, which is a reasonable characteristic of

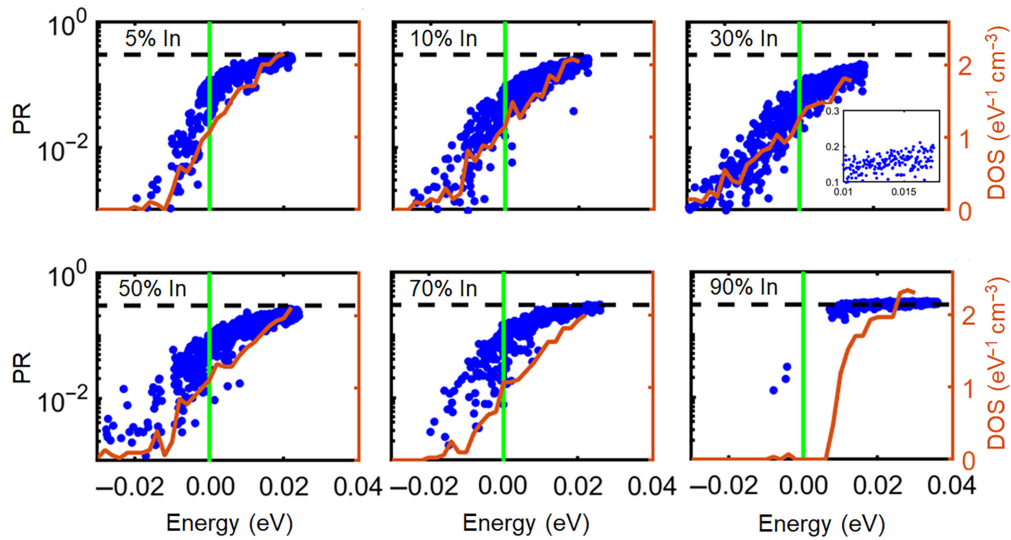


FIG. 14. Dependence of the participation ratio on eigenenergy of the hole eigenstates for different $\text{In}_x\text{Ga}_{1-x}\text{N}$ compositions (log scale) for $x = 0.05, 0.10, 0.30, 0.50, 0.70, 0.90$. The green line represents the valence-band minimum averaged over the structure. The average valence-band maximum value is indicated by the green vertical line and the dashed line represents the PR value of 0.3. Note that below the valence-band maximum, the eigenstates quickly reach low PR values, indicating that they are localized. The red line plotted is the density of states. The inset for $[\text{In}] = 30\%$ shows at an extended scale the PR for delocalized states, somewhat below 0.3 (see text).

a localized state. Plots are then made of the localization length for $\text{In}_x\text{Ga}_{1-x}\text{N}$ hole and electron eigenstates of different energies. These plots are then compared for different indium compositions. Figures 16 and 17 show the dependence on eigenenergy of the localization length for $\text{In}_x\text{Ga}_{1-x}\text{N}$ electron and hole eigenstates. As with the PR plots, the electron eigenstates in Fig. 16 are found to be almost always delocalized at a localization length of 20 nm. The reason ℓ peaks at this value instead of 30 nm, which is the total length of the cube, is that the peak PR value of 0.3 corresponds to an ℓ value of 20 nm. In the case of the holes, the eigenstates in Fig. 17 are found to be localized at the lowest energies. Moreover, as with the

previous PR plots, the number of localized states peaks at 30% indium before falling off again.

The density of states with a localization length below 5 nm (i.e., the density of localized states) is calculated for different In compositions and plotted in Fig. 18. This is done by calculating the number of states that have $\ell < 5$ nm and then dividing that value by the volume of the system ($30 \times 30 \times 30 \text{ nm}^3$). The error bars for each composition are calculated by taking the root-mean-square of ten different configurations of $\text{In}_x\text{Ga}_{1-x}\text{N}$ for the holes and five different ones for electrons. It is observed that there are no localized states for the electrons at any indium composition. On the other hand, the hole eigenstates follow

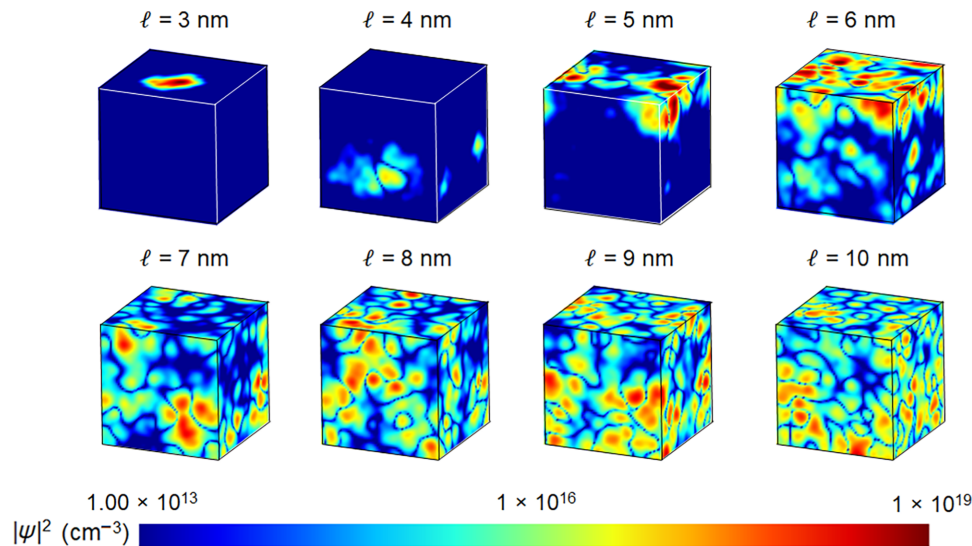


FIG. 15. Probability densities of hole wave functions for $\text{In}_x\text{Ga}_{1-x}\text{N}$ at localization lengths from 3 to 10 nm.

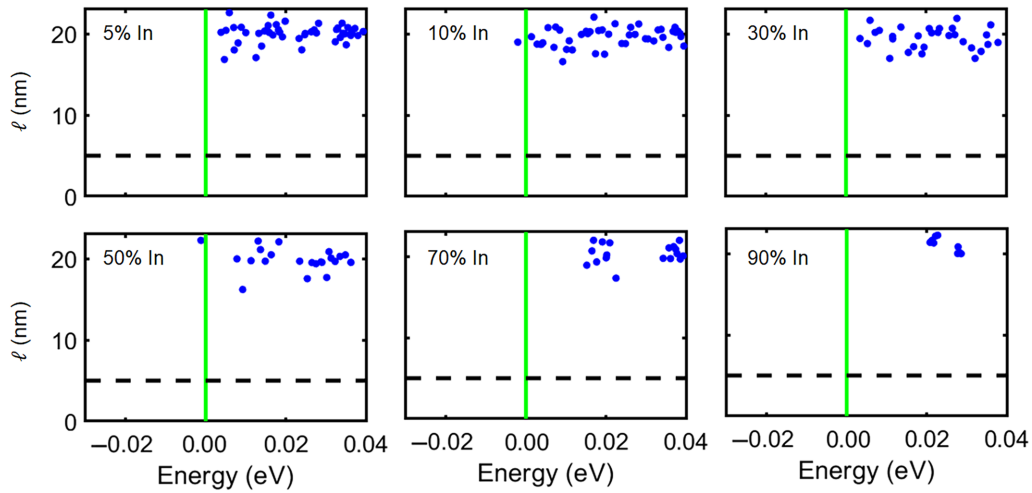


FIG. 16. Localization length of electron wave functions for $\text{In}_x\text{Ga}_{1-x}\text{N}$ for alloy compositions $x = 0.05, 0.10, 0.30, 0.50, 0.70,$ and 0.90 . The green line represents the conduction-band minimum averaged over the structure and the dashed line represents the ℓ value of 5 nm corresponding to the upper value for localized states.

the trend observed earlier, with the highest density of localized hole states for the around 30% $\text{In}_x\text{Ga}_{1-x}\text{N}$ alloy, which confirms our earlier observations. This result correlates with previous studies, which utilize tight-binding models in investigating the behavior of carrier localization in $\text{In}_x\text{Ga}_{1-x}\text{N}$ [10,11], despite our assumption of a one-valence-band model.

VII. OBSERVABILITY OF CARRIER LOCALIZATION IN NITRIDES AND IMPACT ON DEVICES

We now have a detailed knowledge of the localization of carriers in nitride semiconductors, which we can use to assess any observable effects, particularly in devices. For electrons alone, we do not expect localization and carrier transport to be described perturbatively to a good

approximation. This is indeed observed in high electron mobility transistor electron devices with high electron concentrations [32]. On the other hand, hole transport measurements, which would display localization effects, especially at low carrier densities, would be very difficult to perform, due to the low mobility in thin p channels (alloy thickness being growth-limited).

However, carrier localization has recently been observed in a situation where both electrons and holes are present. The localization of electrons bound to localized holes through the Coulomb interaction was revealed in photoemission experiments from p -type $\text{In}_x\text{Ga}_{1-x}\text{N}$ layers: at low temperatures, photoexcited electrons bind to localized holes, as revealed by the strong decrease in photoemission current compared to room temperature [33]. While we do not expect electrons to be localized on their own due to their delocalized wave functions, electrons can be bound to

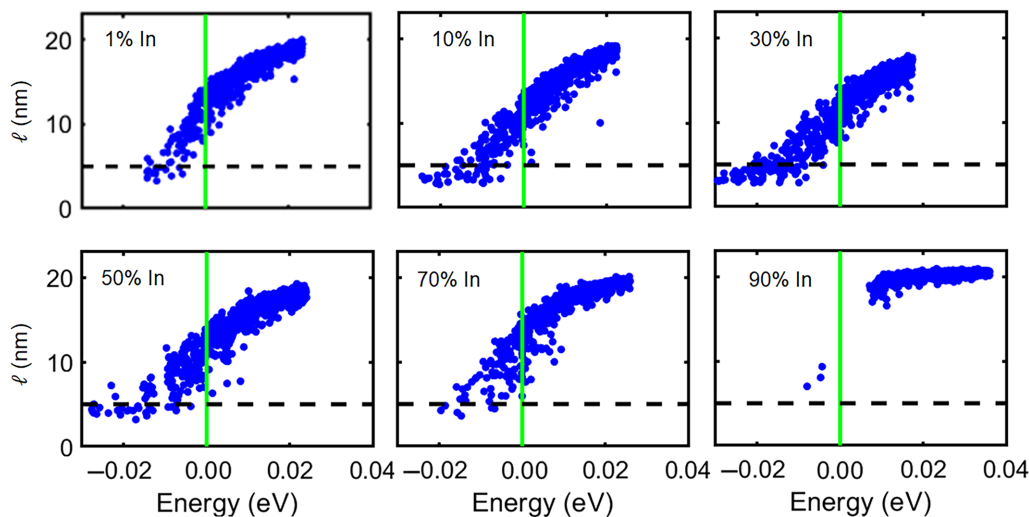


FIG. 17. Localization length of hole wave functions for $\text{In}_x\text{Ga}_{1-x}\text{N}$ $x = 0.05, 0.10, 0.30, 0.50, 0.70,$ and 0.90 . The green line represents the valence-band maximum averaged over the structure and the dashed line represents the ℓ value of 5 nm.

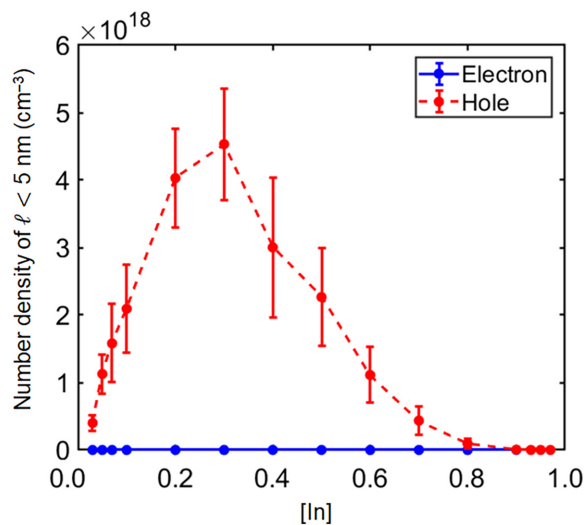


FIG. 18. Density of states with a localization length $\ell < 5$ nm for electron and hole eigenstates at different indium compositions.

localized holes, forming excitonic-like states. However, at room temperature, electrons and holes have weak enough binding energies to be easily unbound. This was computed in detail by David and Weisbuch [34], who showed excitation energies of the bound electron-hole pair in the 20-meV range. The impact of the disorder size was well observed with localization at low temperatures occurring down to 5% In concentration, but disappearing at 2% concentration at which most holes are delocalized (Fig. 18) and the few localized holes are not numerous enough to localize electrons before they escape [33].

Light-emitting devices operate at room temperatures and high carrier concentrations, above $5 \times 10^{18} \text{ cm}^{-3}$. As seen in Figs. 14 and 17, most localized hole states lie within 10–15 meV of delocalized states. Thus, at room temperatures, most of the states are delocalized. In addition, under such concentrations, electron-hole interactions are screened [34], and band filling would also lead to the predominance of unbound states in the transport of both carrier types. Therefore, one should not expect effects of carrier localization in light-emitting devices. This is not to say that disorder does not play any role in such devices: it has been shown that compositional fluctuations and their resulting effective potential play a major role in decreasing the operating voltage in LEDs with multiple quantum wells and other novel transport structures due to the percolating current paths induced in vertical transport [13–15].

VIII. CONCLUSION

By solving the LL and Schrödinger equations, in the envelope wave-function approximation with a single heavy-hole valence band, an analysis is conducted on the localization behavior of carriers in III-nitride and conventional III-V semiconductor alloys

with compositional fluctuations. The landscape potentials obtained are found to have much larger fluctuations in the nitrides due to the larger band gaps and effective masses. Consequently, carriers are likely to be delocalized in the other semiconductors compared with the nitrides. This ties in with observations made on the eigenstate solutions from the Schrödinger equation, which show that both holes and electrons are delocalized in $\text{In}_x\text{Ga}_{1-x}\text{As}$, and by extension, in the other semiconductors. This justifies the perturbative approach of using the virtual-crystal approximation to study carrier transport in conventional III-V semiconductors as the effective masses and band gaps of the aforementioned alloys are much smaller than in nitrides. In the case of $\text{In}_x\text{Ga}_{1-x}\text{N}$, although all the electron eigenstates are shown to be fully delocalized, the lower lying hole eigenstates are not, as evidenced by both visual inspection and through the calculation of the participation ratio as well as the localization length of the eigenstates. In the study of nitride semiconductors, accounting for alloy disorder is necessary to capture the quantum mechanical behavior of carriers when studying their transport mechanisms, given the size of the effective energy landscapes, at least at low carrier densities. While the Schrödinger equation gives exact results, solving the LL equation is a computationally faster method of predicting carrier behavior. This study shows that the solution of the novel LL equation is an elegant method and provides a remarkable view of the impact of compositional disorder in many semiconductors. Thus far, it has also provided the only path to full 3D computations of light-emitting devices [13] and other novel transport structures [14,15] that include alloy disorder.

ACKNOWLEDGMENTS

This work was supported by Collaborative Research in Engineering, Science and Technology (CREST), the Simons Foundation (Grants No. 601952, No. 1027114, and No. 1027116 for J.S.S., C.W., and M.F., respectively), Air Force Office of Scientific Research (Program No. FA9550-19-1-10090), National Science Foundation (NSF) RAISE program (Grant No. A007231601), Sandia National Laboratory (Grant No. 2150283), French National Research Agency (ANR, TECCLON Grant No. ANR-20-CE05-0037-01), and Ministry of Science and Technology, Taiwan (Grants No. MOST 112-2923-E-002-002-, No. MOST 111-2221-E-002-075-, No. MOST 111-2923-E-002-009-, and No. MOST 110-2917-I-002-022).

- [1] T.-P. Lee, Recent advances in long-wavelength semiconductor lasers for optical fiber communication, *Proc. IEEE* **79**, 253 (1991).
- [2] T. Pearsall, M. Piskorski, A. Brochet, and J. Chevrier, A $\text{Ga}_{0.47}\text{In}_{0.53}\text{As}/\text{InP}$ heterophotodiode with reduced dark current, *IEEE J. Quantum Electron.* **17**, 255 (1981).

- [3] S. Nakamura, M. Senoh, N. Iwasa, and S. N. S. Nagahama, High-brightness InGaN blue, green and yellow light-emitting diodes with quantum well structures, *Jpn. J. Appl. Phys.* **34**, L797 (1995).
- [4] P. Li, H. Li, Y. Yao, H. Zhang, C. Lynsky, K. S. Qwah, J. S. Speck, S. Nakamura, and S. P. DenBaars, Demonstration of high efficiency cascaded blue and green micro-light-emitting diodes with independent junction control, *Appl. Phys. Lett.* **118**, 261104 (2021).
- [5] C. Weisbuch, S. Nakamura, Y.-R. Wu, and J. S. Speck, Disorder effects in nitride semiconductors: Impact on fundamental and device properties, *Nanophotonics* **10**, 3 (2021).
- [6] C. Kittel and P. McEuen, *Introduction to Solid State Physics* (John Wiley & Sons, Limited, New York, 2018).
- [7] L. Bellaiche, T. Mattila, L.-W. Wang, S.-H. Wei, and A. Zunger, Resonant hole localization and anomalous optical bowing in InGaN alloys, *Appl. Phys. Lett.* **74**, 1842 (1999).
- [8] P. R. C. Kent and A. Zunger, Carrier localization and the origin of luminescence in cubic InGaN alloys, *Appl. Phys. Lett.* **79**, 1977 (2001).
- [9] D. Watson-Parris, M. J. Godfrey, P. Dawson, R. A. Oliver, M. J. Galtrey, M. J. Kappers, and C. J. Humphreys, Carrier localization mechanisms in $\text{In}_x\text{Ga}_{1-x}/\text{GaN}$ quantum wells, *Phys. Rev. B* **83**, 115321 (2011).
- [10] S. Schulz, M. A. Caro, C. Coughlan, and E. P. O'Reilly, Atomistic analysis of the impact of alloy and well-width fluctuations on the electronic and optical properties of InGaN/GaN quantum wells, *Phys. Rev. B* **91**, 035439 (2015).
- [11] D. S. P. Tanner, P. Dawson, M. J. Kappers, R. A. Oliver, and S. Schulz, Polar (In, Ga)N/GaN quantum wells: Revisiting the impact of carrier localization on the “green gap” problem, *Phys. Rev. Appl.* **13**, 044068 (2020).
- [12] M. Filoche, M. Piccardo, Y.-R. Wu, C.-K. Li, C. Weisbuch, and S. Mayboroda, Localization landscape theory of disorder in semiconductors. I. Theory and modeling, *Phys. Rev. B* **95**, 144204 (2017).
- [13] C. K. Li, M. Piccardo, L. S. Lu, S. Mayboroda, L. Martinelli, J. Peretti, J. S. Speck, C. Weisbuch, M. Filoche, and Y. R. Wu, Localization landscape theory of disorder in semiconductors. III. Application to carrier transport and recombination in light emitting diodes, *Phys. Rev. B* **95**, 144206 (2017).
- [14] K. S. Qwah, M. Monavarian, G. Lheureux, J. Wang, Y.-R. Wu, and J. S. Speck, Theoretical and experimental investigations of vertical hole transport through unipolar AlGaIn structures: Impacts of random alloy disorder, *Appl. Phys. Lett.* **117**, 022107 (2020).
- [15] K. S. Qwah, M. Monavarian, W. Y. Ho, Y.-R. Wu, and J. S. Speck, Vertical hole transport through unipolar InGaIn quantum wells and double heterostructures, *Phys. Rev. Mater.* **6**, 044602 (2022).
- [16] J. M. Luttinger and W. Kohn, Motion of electrons and holes in perturbed periodic fields, *Phys. Rev.* **97**, 869 (1955).
- [17] G. Bastard, *Wave Mechanics Applied to Semiconductor Heterostructures* (Les Editions de Physique, Paris, 1990).
- [18] J.-P. Banon, P. Pelletier, C. Weisbuch, S. Mayboroda, and M. Filoche, Wigner-Weyl description of light absorption in disordered semiconductor alloys using the localization landscape theory, *Phys. Rev. B* **105**, 125422 (2022).
- [19] M. Piccardo, C.-K. Li, Y.-R. Wu, J. S. Speck, B. Bonef, R. M. Farrell, M. Filoche, L. Martinelli, J. Peretti, and C. Weisbuch, Localization landscape theory of disorder in semiconductors. II. Urbach tails of disordered quantum well layers, *Phys. Rev. B* **95**, 144205 (2017).
- [20] C. M. Jones, C.-H. Teng, Q. Yan, P.-C. Ku, and E. Kioupakis, Impact of carrier localization on recombination in InGaN quantum wells and the efficiency of nitride light-emitting diodes: Insights from theory and numerical simulations, *Appl. Phys. Lett.* **111**, 113501 (2017).
- [21] See Supplemental Material at <http://link.aps.org/supplemental/10.1103/PhysRevApplied.20.044069> for details on the participation ratio, the localization length, comparisons to tight-binding and $\mathbf{k}\cdot\mathbf{p}$ calculations, and the justification for using a single heavy-hole valence band.
- [22] M. Filoche and S. Mayboroda, Universal mechanism for Anderson and weak localization, *PNAS* **109**, 14761 (2012).
- [23] D. N. Arnold, G. David, D. Jerison, S. Mayboroda, and M. Filoche, Effective confining potential of quantum states in disordered media, *Phys. Rev. Lett.* **116**, 056602 (2016).
- [24] *Optoelectronic Device Simulation Laboratory—光電元件模擬軟體開發實驗室*, <http://yrwu-wk.ee.ntu.edu.tw/>.
- [25] E. Anderson, Z. Bai, C. Bischof, L. S. Blackford, J. Demmel, J. Dongarra, J. Du Croz, A. Greenbaum, S. Hammarling, A. McKenney, and D. Sorensen, *LAPACK Users' Guide* (Society for Industrial and Applied Mathematics, Philadelphia, 1999).
- [26] E. O. Kane, Band structure of indium antimonide, *J. Phys. Chem. Solids* **1**, 249 (1957).
- [27] C. Hermann and C. Weisbuch, $\mathbf{k}\cdot\mathbf{p}$ perturbation theory in III-V compounds and alloys: A reexamination, *Phys. Rev. B* **15**, 823 (1977).
- [28] L.-W. Wang, Calculations of carrier localization in $\text{In}_x\text{Ga}_{1-x}\text{N}$, *Phys. Rev. B* **63**, 245107 (2001).
- [29] S. Hammersley, D. Watson-Parris, P. Dawson, M. J. Godfrey, T. J. Badcock, M. J. Kappers, C. McAleese, R. A. Oliver, and C. J. Humphreys, The consequences of high injected carrier densities on carrier localization and efficiency droop in InGaIn/GaN quantum well structures, *J. Appl. Phys.* **111**, 083512 (2012).
- [30] J. A. Chan, J. Z. Liu, and A. Zunger, Bridging the gap between atomic microstructure and electronic properties of alloys: The case of (In, Ga)N, *Phys. Rev. B* **82**, 045112 (2010).
- [31] R. J. Bell and P. Dean, Atomic vibrations in vitreous silica, *Discuss. Faraday Soc.* **50**, 55 (1970).
- [32] P. Sohi, J.-F. Carlin, and N. Grandjean, Alloy disorder limited mobility of InGaIn two-dimensional electron gas, *Appl. Phys. Lett.* **112**, 262101 (2018).
- [33] Mylène Sauty, Nicolas M. S. Lopes, Jean-Philippe Banon, Yves Lassailly, Lucio Martinelli, Abdullah Alhassan, Yi Chao Chow, Shuji Nakamura, James S. Speck, Claude Weisbuch, and Jacques Peretti, Localization effect in photoelectron transport induced by alloy disorder in nitride semiconductor compounds, *Phys. Rev. Lett.* **129**, 216602 (2022).
- [34] A. David and C. Weisbuch, Excitons in a disordered medium: A numerical study in InGaIn quantum wells, *Phys. Rev. Res.* **4**, 043004 (2022).